

# 4D-RaDiff: Latent Diffusion for 4D Radar Point Cloud Generation

Jimmie Kwok<sup>1,2</sup>

Holger Caesar<sup>1</sup>

Andras Palffy<sup>2</sup>

<sup>1</sup>Delft University of Technology

<sup>2</sup>Perciv AI

## Abstract

Automotive radar has shown promising developments in environment perception due to its cost-effectiveness and robustness in adverse weather conditions. However, the limited availability of annotated radar data poses a significant challenge for advancing radar-based perception systems. To address this limitation, we propose a novel framework to generate 4D radar point clouds for training and evaluating object detectors. Unlike image-based diffusion, our method is designed to consider the sparsity and unique characteristics of radar point clouds by applying diffusion to a latent point cloud representation. Within this latent space, generation is controlled via conditioning at either the object or scene level. The proposed 4D-RaDiff converts unlabeled bounding boxes into high-quality radar annotations and transforms existing LiDAR point cloud data into realistic radar scenes. Experiments demonstrate that incorporating synthetic radar data of 4D-RaDiff as data augmentation method during training consistently improves object detection performance compared to training on real data only. In addition, pre-training on our synthetic data reduces the amount of required annotated radar data by up to 90% while achieving comparable object detection performance.

## 1. Introduction

Robust perception is crucial for autonomous vehicles to understand their surroundings and make safe driving decisions. Automotive sensors such as cameras and LiDAR have become the predominant choices for perceiving the environment. However, both sensor types show reduced reliability in adverse weather conditions, including rain, fog, or snow. Camera sensors are also negatively affected in low-light environments [58].

In recent years, 4D millimeter-wave radar has emerged as a promising alternative sensor modality. The longer wavelengths of radar allow it to penetrate atmospheric particles, making it suitable for harsh environmental conditions [42]. Modern automotive radars provide processed data in the form of point clouds, with the distinctive ability to

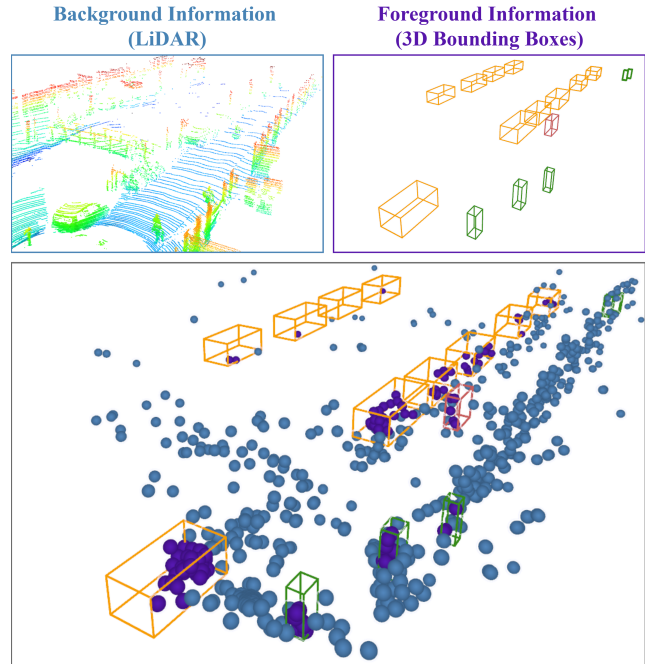


Figure 1. 4D-RaDiff separately generates background (blue) and foreground (purple) radar points by conditioning on LiDAR and 3D bounding boxes, respectively. Background and foreground points can be fused to form a complete synthetic 4D radar point cloud.

also measure the relative radial velocity of an object via the Doppler effect. The inclusion of Doppler information has been shown to significantly improve the performance of radar-based object detection [31, 32].

Despite the unique attributes of radar, its perception capabilities still fall short of established LiDAR-based methods [1, 32]. This performance gap can be mainly attributed to two key factors: the inherent sparsity of radar point clouds and the limited availability of annotated radar data [5, 41, 66]. While many studies have focused on obtaining denser representations of radar point clouds through generative [25, 50, 62] or other learning-based approaches [11, 36], they often overlook the scarcity of radar annota-

tions. Acquiring such annotations is labor-intensive, time-consuming, and costly, as it demands extensive effort in data collection, synchronization, and manual labeling.

To alleviate this problem, we propose 4D-RaDiff, a novel latent diffusion framework for 4D radar point cloud generation designed for downstream tasks, enabling synthetic data to be readily used for training radar perception models. As shown in Fig. 1, we produce the synthetic data in two ways: (1) synthesizing foreground points within annotated 3D bounding boxes, and (2) generating background points conditioned on LiDAR point clouds to capture scene-level context outside the annotated regions. We disentangle the generation process because foreground and background radar points follow different distributions. Foreground points correspond to semantic objects, often dynamic in nature and composed of distinct reflective surfaces, whereas background points are largely static and dominated by noise and clutter. Therefore, modeling each component separately enables high-fidelity generation tailored to their underlying characteristics.

To model radar point clouds effectively, we operate directly on a point-based latent representation rather than converting them to images. Image representations of point clouds [15, 25, 27, 35, 67] are widely used, as they allow the use of conventional image-based diffusion methods. However, radar data produces extremely sparse images, limiting their applicability. While applying diffusion directly on the points [30] could overcome this problem, modeling the irregular distribution of all radar features remains challenging. To address these design considerations, we first train a point-based variational autoencoder (VAE) to map the radar points to a regularized latent point cloud space. Subsequently, a diffusion model is trained on the latent representations, conditioned on the relevant inputs. In contrast to previous generative models for radar point clouds [25, 51, 62] that synthesize only spatial features, our method also generates radar-specific characteristics, i.e., Doppler and radar cross-section (RCS). Another related method [46] simulates radar points and all of their features, but relies on a discriminative approach, constraining both the diversity and the capability to generate novel radar data.

Given that 4D-RaDiff is the first method of its kind, we validate its effectiveness by evaluating how well synthetic data generated by our approach improves radar-based 3D object detection. We conduct experiments by training jointly on synthetic and real data via data augmentation, and by pre-training on synthetic data followed by fine-tuning on real data.

In summary, our work consists of the following key contributions:

- We propose 4D-RaDiff, the first latent diffusion framework operating directly on a point-based radar representation, allowing for the generation of 4D radar point clouds

including Doppler and RCS features.

- We introduce a foreground–background generation pipeline, where foreground radar points are generated conditioned on 3D bounding boxes, and background points are synthesized using LiDAR data as conditioning.
- We demonstrate that our framework improves radar-based 3D object detection performance on the View-of-Delft [32] and TruckScenes [6] datasets, using synthetic data for either data augmentation or pre-training.

## 2. Related Work

**Data Augmentation** artificially inflates the size and diversity of the training dataset, thereby reducing overfitting, improving generalization, and enhancing model performance. In the image domain, augmentation techniques have been extensively studied [44], whereas data augmentation for point clouds remains relatively underexplored. Basic augmentation methods originally developed for images can also be applied to point cloud data. Common examples are flipping, scaling, rotation, translation, adding random noise, and randomly dropping points. Inspired by mix-based image augmentations [7, 59, 60], GT-Sampling [55] inserts ground truth objects, sampled from a database constructed prior to training, by copy-pasting them into training samples. The downside of GT-Sampling is that it may still place objects in unreasonable locations, causing either occlusion or collision with the environment. Thus, several improved variants [4, 16, 23] have been implemented to address these issues. Other augmentations simulate the effects of adverse weather on LiDAR point clouds [8, 9, 19]. Despite the existing work on point cloud augmentations, many of the methods were designed for LiDAR point cloud data. For instance, [32] highlights the potential risks of applying simple augmentation strategies to radar point clouds, as they may distort the Doppler feature of the points. Consequently, there is a need for advanced methods that can augment radar point clouds in a way that preserves their semantic features.

**Diffusion Models** have garnered significant interest because of their impressive results in image generation [3, 14, 29, 45, 47]. The generation process can be guided by providing conditional information, facilitating tasks such as class-conditional image generation [3, 18], text-to-image generation [28, 34, 40], and image-to-image translation [2, 39]. One shortcoming of diffusion models is their high demand for computational resources, particularly when operating in the high-dimensional space of images, which results in prolonged training and inference times. To mitigate this issue, Latent Diffusion Models (LDMs) [38] apply the diffusion process in a lower-dimensional latent space, which significantly improves efficiency while retaining generation quality.

**LiDAR-based Diffusion Models** extend the diffusion process to LiDAR point cloud data. The most common data representation of LiDAR points is an image representation, which allows standard image-based diffusion methods to be applied. Both [27] and [13] focus on LiDAR point cloud upsampling by formulating it as an image inpainting task, where the sparse point cloud serves as the inpainting mask. LidarDM [67], LiDMs [35], and RangeLDM [15] leverage LDMs to generate LiDAR scenes. LidarDM synthesizes temporally coherent LiDAR sequences conditioned on semantic layout maps. LiDMs are capable of generating LiDAR point clouds from multi-modal conditions (e.g., semantic maps, camera views, and text prompts). RangeLDM addresses the tasks of LiDAR point cloud upsampling and inpainting. Instead of representing LiDAR point clouds as an image, [30] applies diffusion directly on the points to generate a more dense LiDAR scene. Other point-based diffusion methods [21, 53] generate LiDAR point clouds for individual objects rather than entire scenes. In contrast, we operate the diffusion process within a learned latent point cloud representation, which better preserves the unique properties of radar data.

**Radar-based Diffusion Models** operate on radar data, represented as either a tensor or point cloud. The radar tensor contains power measurements across spatial and Doppler domains and can be interpreted as an image. To obtain the radar point cloud, the Constant False Alarm Rate (CFAR) algorithm is typically applied on this low-level data. Most radar diffusion methods aim to generate denser radar point clouds, using LiDAR as supervision while conditioning on either radar tensor [49, 56, 62] or radar point cloud [25, 50, 51, 64]. Sem-RaDiff [61] exploits both radar point cloud and tensor information to derive an intermediate representation, which is then used as a conditional input for the diffusion model to generate LiDAR-like point clouds with semantic labels. However, the aforementioned methods fail to generate key radar features, such as Doppler and RCS, since they are designed to produce point clouds similar to LiDAR. Furthermore, our method generates radar point clouds from scratch, requiring no radar data as conditioning input.

### 3. Method

In this section, we describe the overall pipeline of the proposed 4D-RaDiff, as shown in Fig. 2.

#### 3.1. Latent Point Diffusion Model

To address the sparsity of radar point clouds and the highly irregular distribution of their features, existing methods, i.e., image-based diffusion [15, 25, 27, 35, 67] and diffusion in the original point cloud space [21, 30] may not be well suited to handle these limitations. We circumvent these

challenges by applying diffusion that operates within a regularized latent point cloud representation of radar points. To this end, we design a point-based VAE built upon [12], and use Sparse Point-Voxel Diffusion (SPVD) [37] as the backbone of our model.

First, we train a VAE to encode the radar point cloud representation into a regularized latent point cloud space. The training objective consists of a reconstruction loss and Kullback-Leibler regularization. The input to the VAE is a radar point cloud, represented as a set of  $N$  points with xyz-coordinates, Doppler and RCS as its features, and is denoted as  $x \in \mathbb{R}^{N \times 5}$ . The encoder  $\mathcal{E}$  maps the radar point cloud  $x$  to a latent representation  $z = \mathcal{E}(x)$ , where  $z \in \mathbb{R}^{M \times d_z}$ . The decoder aims to reconstruct the original point cloud from the latent,  $\tilde{x} = \mathcal{D}(z) = \mathcal{D}(\mathcal{E}(x))$ . The full training objective and model architecture of the VAE are provided in the supplement.

In the second stage, we train the model  $\epsilon_\theta$  on the latent space representation  $z$ , where the VAE’s encoder and decoder are kept frozen. We follow the standard formulation of denoising diffusion probabilistic models [14], with derivations provided in our supplementary material. The objective of our LDM is defined as follows:

$$L_{\text{LDM}} = \mathbb{E}_{\mathcal{E}(x), y, \epsilon \sim \mathcal{N}(0, I), t} \left[ \|\epsilon - \epsilon_\theta(z_t, t, \tau_\theta(y))\|_2^2 \right]. \quad (1)$$

Given a condition  $y$ , the model  $\epsilon_\theta$  predicts the noise  $\epsilon$  that has been added to the latent point cloud  $z_0$  to produce the noisy latent  $z_t$  after  $t$  forward diffusion steps. We jointly optimize the denoising network  $\epsilon_\theta$  and the encoder  $\tau_\theta$  of the conditioning mechanism, where a separate encoder is designed for each type of conditioning input.

#### 3.2. Foreground Generation

Foreground points are defined as the points that lie within the annotated 3D bounding boxes representing road users. Our model generates these points by conditioning on the bounding boxes of the scene. To achieve this, we apply a cross-attention mechanism [48] at multiple layers within the backbone of the LDM.

For the representation and encoder of the bounding boxes, we implement a strategy similar to LayoutDiffusion [65], extending their approach from 2D to 3D bounding boxes. Specifically, we define a fixed set of  $n$  objects, denoted as  $\mathcal{S} = \{o_0, o_1, \dots, o_{n-1}\}$ . Each object is given by  $o_i = \{b_i, c_i\}$ , where  $b_i \in [0, 1]^9$  is a vector representing the position, size, yaw and 2D velocities of a bounding box and  $c_i \in [0, C + 1]$  denotes its class id. We incorporate additional features such as the yaw angle and bounding box velocities, because they provide crucial information for the synthesis of radar point clouds with accurate Doppler values. Consistent with the design of LayoutDiffusion, the first object  $o_0$  of the set  $\mathcal{S}$  is always a fixed representation with

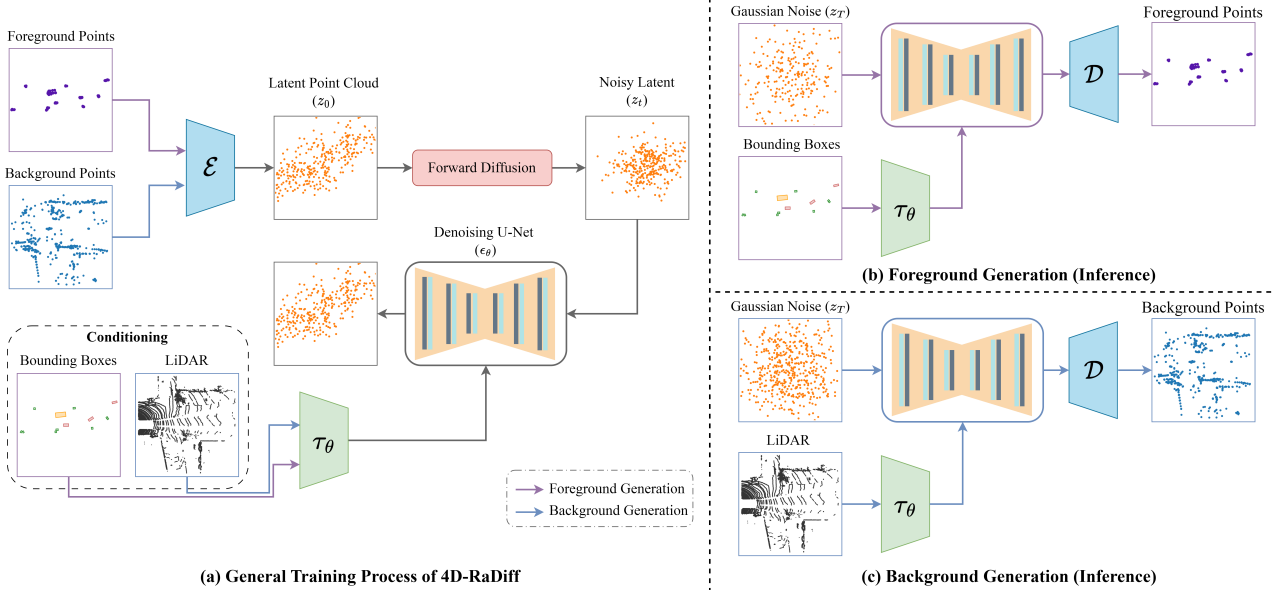


Figure 2. **The overall framework of 4D-RaDiff.** (a) During the training phase, we encode each radar point cloud with the frozen point-based encoder  $\mathcal{E}$  of the variational autoencoder into a latent point cloud representation. We train two separate latent diffusion models (LDMs) and their respective conditioning encoder  $\tau_\theta$ , each tailored to the specific task of either foreground (c.f. Sec. 3.2) or background (c.f. Sec. 3.3) generation. During inference, the LDM generates foreground points (b) conditioned on 3D bounding boxes, or background points (c) conditioned on the LiDAR point cloud.

$c_0 = 0$ , where  $b_0$  corresponds to a bounding box covering the entire point cloud range. This fixed representation provides global scene context for conditioning. To ensure a fixed sequence length of  $n$  objects in each frame, we pad the set with empty objects  $o_p$  when necessary, which consists of a zero vector for  $b_p$  and class id  $c_p = C + 1$ .

The encoder processes the input set  $\mathcal{S}$  by separately embedding the bounding box and class information for each object and summing them to produce the initial layout embeddings. To encourage the interaction between the different objects, the layout fusion module introduced in [65] applies multiple layers of self-attention to these embeddings. The embedding corresponding to  $o_0$ , which encodes the overall bounding box layout, is used for global conditioning. Subsequently, the embeddings of the objects are fed into the cross-attention layers of the LDM for local conditioning.

### 3.3. Background Generation

Background points consist of all points in the point cloud that are not classified as foreground points. The generated background points are merged with foreground points to form a complete radar point cloud, which can then be used for downstream tasks. To generate background points, we condition solely on the LiDAR point cloud of the scene. This design choice is motivated by the fact that LiDAR provides a highly accurate representation of the background

environment, and most 4D radar point cloud datasets provide both radar and LiDAR modalities. In contrast, alternative sources for background conditioning, such as high-definition maps, are typically not available. Furthermore, this approach enables extending existing datasets that contain only LiDAR data with synthetic radar point clouds.

We employ PointPillars [22] to map the LiDAR point cloud to an intermediate representation, which serves as input to the model’s cross-attention layers. For each LiDAR scan, we consider only points located within the same spatial range as the radar point cloud.

## 4. Experiments

**Datasets.** For our experiments, we used the View-of-Delft (VoD) [32] and TruckScenes [6] dataset. The VoD dataset provides synchronized and calibrated sensor data captured in Delft, which consists of LiDAR point clouds, camera images, and 4D radar point clouds captured from a single front-facing radar sensor. It also contains 3D bounding box annotations, including labels for cars, cyclists, and pedestrians. Although VoD is relatively limited in scale, the TruckScenes dataset offers a much larger and more diverse data collection. The data was primarily recorded on German highways by a truck, obtained using four cameras, six LiDAR, and six radar sensors. It also provides 4D radar point clouds with 360-degree coverage and a broader set of class labels, with an annotation range up to 150 m.

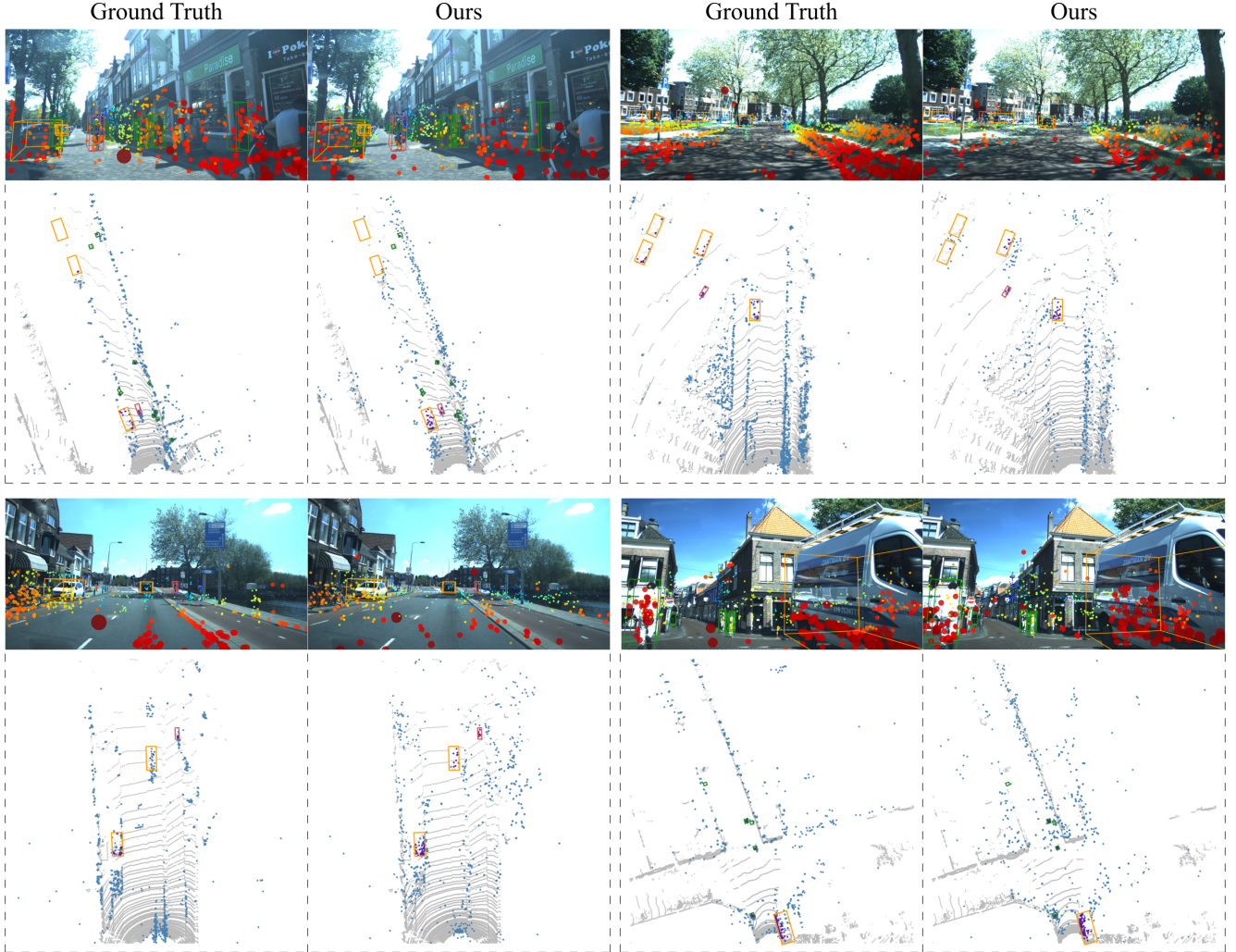


Figure 3. Qualitative results of 4D radar point cloud generation on the VoD dataset. Each camera image shows the radar point clouds projected onto it, while the corresponding bottom image represents the radar point clouds in a Bird’s-Eye View (BEV) of the same scene. In the BEV image, radar point clouds are distinguished as foreground (purple) and background (blue). 3D bounding boxes are displayed in orange for cars, red for cyclists, and green for pedestrians. LiDAR point clouds are included in the BEV images for reference only.

**Baselines.** To the best of our knowledge, there is no previous work that generates 4D radar point clouds, including Doppler and RCS features, from either 3D bounding box annotations or LiDAR data. Therefore, we evaluate the effectiveness of 4D-RaDiff indirectly, by assessing whether incorporating its synthetic data during training improves performance on a downstream perception task, namely 3D object detection. As baselines, we consider object detectors trained only on real data. We investigate two applications to leverage our synthetic data during training: data augmentation and pre-training solely on synthetic data. For augmentation, we employ GT-Sampling [55], a widely used augmentation technique for LiDAR-based object detection. We compare the object detection performance of models trained solely on real data with models trained on both real and

synthetic data. The object detection models for these experiments include CenterPoint [57], PointPillars [22], and PillarNet [43].

**Implementation Details.** We train our foreground and background generation models separately on a single RTX 4090 GPU. We train each diffusion model for 1000 epochs using a one-cycle learning rate policy, with a max learning rate of  $1e-4$ . For the diffusion process, we use a linear noise schedule with  $T = 1000$  diffusion steps, where  $\beta_0 = 1e-4$  and  $\beta_T = 2e-2$ . Given the sparsity of radar data, we aggregate multiple radar sweeps for all experiments, following [32] and [6]. Furthermore, all object detectors are trained with standard global augmentations by default, including random horizontal flip, global rotation within  $[-\pi/4, \pi/4]$ , and global scaling in the range of



Figure 4. Qualitative example of generated radar points for an object from the VoD validation set. Both real and synthetic points of the black car in front of the ego vehicle are plotted in top view, colored by either Doppler or RCS.

[0.95, 1.05]. Additional details about the implementation can be found in Appendix C.

**Evaluation Metrics.** To assess the generative performance of our method, we use Chamfer Distance (CD) to measure the spatial similarity between generated and real radar point clouds. Moreover, we introduce radar-specific metrics,  $CD_{\text{Doppler}}$  and  $CD_{\text{RCS}}$ , which quantify the fidelity of the generated Doppler and RCS values, respectively. Please refer to the supplementary material for detailed definitions. For evaluating object detection performance, the VoD dataset uses average precision (AP) with IoU thresholds of 0.5 for cars, and 0.25 for cyclists and pedestrians. VoD also reports metrics for two regions: (1) entire annotated area (camera FoV up to 50 meters) and (2) driving corridor, a safety-critical region located in front of the ego vehicle defined as  $[-4 \text{ m} < x < 4 \text{ m}, 0 < z < 25 \text{ m}]$  in camera coordinates. Detection performance on the TruckScenes dataset is measured by a distance-based AP for each class and the nuScenes Detection Score (NDS) [1].

#### 4.1. Augmenting Real Data with Synthetic Data

In this experiment, we evaluate the quality of our generated foreground points by measuring the performance of an object detector when using these points for augmentation

during training. To achieve this, we generate foreground points for the car, cyclist, and pedestrian classes, ensuring a consistent approach across datasets. We use GT-Sampling [55] to insert synthetic radar points and their corresponding bounding boxes into training samples. A comparable experiment with synthetic data using GT-Sampling has been explored in [17], but our method applies the augmentation strategy to radar point clouds, in contrast to radar tensor data. GT-sampling creates a database prior to training, storing foreground points and bounding boxes from the training dataset. During training, points and their associated bounding boxes are randomly sampled from the database and inserted at their original positions into the point clouds of different scenes. A collision check is performed after insertion to remove any sampled boxes and points that overlap with existing bounding boxes.

Tab. 1 reports the object detection performance of CenterPoint [57] on the VoD dataset, comparing the effects of GT-Sampling using only real data, only synthetic data, or a combination of both. Using synthetic data alone for GT-Sampling results in slightly lower performance compared to sampling from real data, indicating that our generated object-level radar points closely resemble real points in terms of their effectiveness for training. The best performance is achieved when both real and synthetic data are used jointly as augmentation strategy, demonstrating the benefit of our generative model for improving existing augmentation methods.

To showcase the versatility of our method, we conduct a similar study on the TruckScenes dataset involving multiple object detectors such as CenterPoint [57], PointPillars [22], and PillarNet [43]. TruckScenes contains a larger variety of class labels than VoD, but also suffers from class imbalance, with cars accounting for 46.09%, pedestrians 1.50%, and bicycles only 0.16% of all training labels. To mitigate this, we generate foreground points for all three classes, with particular emphasis on oversampling the underrepresented pedestrian and bicycle categories. As shown in Tab. 2, incorporating our synthetic data leads to significant improvements for the rare classes (pedestrians and bicycles), with minor improvements for the car class. Although some classes may experience slight performance drops when including our generated radar points, overall metrics (mAP and NDS) consistently improve across all object detectors.

In Fig. 4, we also show a qualitative example of our generated foreground points for an object in the VoD validation set. Qualitative examples of synthetic radar points for various objects from the TruckScenes dataset can be found in Appendix E.

#### 4.2. Pre-Training on Synthetic Data

We evaluate the quality of both our generated background and foreground points on the VoD dataset by pre-training

Table 1. 3D object detection performance on the VoD validation set. Metrics are reported for the entire annotated area and the driving corridor. For the real and synthetic setting, the database of each contains the same amount of bounding boxes.

Category	Method	Entire Annotated Area				Driving Corridor			
		mAP	AP <sub>car</sub>	AP <sub>cyc</sub>	AP <sub>ped</sub>	mAP	AP <sub>car</sub>	AP <sub>cyc</sub>	AP <sub>ped</sub>
Baseline (Real)	CenterPoint [57]	46.0	37.9	65.2	34.9	66.2	69.2	86.7	42.8
	CenterPoint + GT-Sampling [55] (real)	52.4	39.9	74.1	43.2	71.0	71.2	91.1	50.8
Ours (Synthetic)	CenterPoint + GT-Sampling (synthetic)	51.2	39.8	71.5	42.3	69.8	72.0	89.5	47.8
	CenterPoint + GT-Sampling (real + synthetic)	<b>53.3</b>	<b>40.5</b>	<b>75.0</b>	<b>44.4</b>	<b>72.5</b>	<b>72.3</b>	<b>93.9</b>	<b>51.2</b>

Table 2. 3D object detection performance on the TruckScenes validation set. The detection range is evaluated up to 75 m for all classes (note that the official range is 150 m for Car, Truck, Trailer, O.V., and Bus). † indicates classes where GT-Sampling is applied in both real (R) and synthetic (S) settings. O.V., Motor., Ped., T.C., T.S. are short for other vehicle, motorcycle, pedestrian, traffic cone and traffic sign, respectively. The official TruckScenes evaluation classes Bus, Barrier, and Animal achieve zero AP for all methods and are omitted from this table, but are included in mAP and NDS calculation.

Method	GT-Sampling [55]	mAP	NDS	Car <sup>†</sup>	Truck	Trailer	O.V.	Ped. <sup>†</sup>	Motor.	Bike <sup>†</sup>	T.C.	T.S.
CenterPoint [57]	R	19.8	27.3	55.2	45.5	<b>56.5</b>	3.5	1.9	36.3	0.0	16.9	<b>22.0</b>
	R+S	<b>20.8</b>	<b>27.9</b>	<b>55.5</b>	<b>46.0</b>	56.3	<b>4.6</b>	<b>4.9</b>	<b>37.5</b>	<b>4.8</b>	<b>18.0</b>	21.7
<i>Improvements</i>		+1.0	+0.6	+0.3	+0.5	-0.2	+1.1	+3.0	+1.2	+4.8	+1.1	-0.3
PointPillars [22]	R	14.7	28.4	48.3	30.5	44.5	1.6	0.0	<b>26.0</b>	0.0	9.9	15.5
	R+S	<b>15.3</b>	<b>29.9</b>	<b>49.7</b>	<b>30.8</b>	<b>45.0</b>	<b>2.1</b>	<b>2.3</b>	24.9	<b>2.6</b>	<b>10.4</b>	<b>15.8</b>
<i>Improvements</i>		+0.6	+1.5	+1.4	+0.3	+0.5	+0.5	+2.3	-1.1	+2.6	+0.5	+0.3
PillarNet [43]	R	20.3	25.3	55.1	<b>46.6</b>	<b>54.5</b>	4.1	2.7	35.4	0.4	<b>18.3</b>	26.3
	R+S	<b>21.0</b>	<b>27.8</b>	<b>55.3</b>	46.3	53.7	<b>4.2</b>	<b>6.2</b>	<b>37.0</b>	<b>4.7</b>	18.1	<b>26.8</b>
<i>Improvements</i>		+0.7	+2.5	+0.2	-0.3	-0.8	+0.1	+3.5	+1.6	+4.3	-0.2	+0.5

an object detector on fully synthetic radar point clouds. In Fig. 3, we showcase examples of synthetic radar point clouds, which combine the generated background and foreground points of 4D-RaDiff. To obtain our synthetic training data, we use LiDAR from the test split (which is not used for official evaluation) combined with global transformations to generate background points, and we sample random bounding boxes to generate foreground points.

The results of pre-training a CenterPoint [57] detector on fully synthetic radar data are presented in Tab. 3. We experiment with different amounts of pre-training data, using the same number of synthetic samples as the actual training set (100%), as well as twice (200%) and three times (300%) that amount. We also investigate several fine-tuning configurations: no fine-tuning, fine-tuning on 10%, and fine-tuning on 100% of annotated training data. For the 10%-configuration, we select every tenth sample from the training data, effectively simulating a 1 Hz annotation frequency (given VoD’s annotation frequency of 10 Hz).

When training exclusively on synthetic data, we observe a significant performance drop compared to training on real data, emphasizing the domain gap between synthetic and real data. As expected, using twice as much synthetic data, the performance of the detector increases. Conversely,

when training on even more synthetic data (300%) the performance does not improve. This suggests that simply increasing the amount of synthetic training data does not always improve performance, as it becomes harder for the model to generalize to real-world data distributions.

Notably, pre-training on synthetic data followed by fine-tuning on just 10% of real data results in substantial performance improvements compared to training solely on synthetic data. More importantly, across all pre-training configurations, the model consistently outperforms the baseline trained solely on the full real training set without any pre-training. This indicates that pre-training on synthetic data can initialize the model weights effectively, enabling it to achieve good performance even in the absence of large annotated data.

Finally, pre-training and fine-tuning on the entire training set achieves the best overall performance. However, the performance gain of using the whole training set (100%) for fine-tuning compared to fine-tuning on a small subset (10%) is not as substantial as one might expect. A plausible explanation is that bridging the synthetic-to-real domain gap requires only a small amount of diverse, real annotated data during fine-tuning, as the model has already learned the fundamental structure of the task during pre-training.

Table 3. Comparison of 3D object detection results on the VoD validation set using CenterPoint [57] under different training strategies. Metrics are reported for the entire annotated area and the driving corridor. Percentage (%) indicates the proportion of samples relative to the full VoD training set (5138 samples).

Category	Method		Entire Annotated Area				Driving Corridor			
	Pre-train (synthetic)	Fine-tune (real)	mAP	AP <sub>car</sub>	AP <sub>cyc</sub>	AP <sub>ped</sub>	mAP	AP <sub>car</sub>	AP <sub>cyc</sub>	AP <sub>ped</sub>
Baseline	0%	100%	46.0	37.9	65.2	34.9	66.2	69.2	86.7	42.8
Synthetic Only	100%	0%	10.8	11.2	10.9	10.4	14.6	25.5	6.4	12.0
	200%	0%	13.6	14.3	13.5	12.9	17.2	28.5	8.2	14.9
	300%	0%	11.0	11.4	11.4	10.2	14.2	24.4	5.6	12.5
Synthetic + Real (10%)	100%	10%	47.0	37.5	66.9	36.7	65.9	69.7	85.2	42.9
	200%	10%	47.6	38.2	67.8	36.9	66.9	70.0	86.1	44.6
	300%	10%	46.5	36.8	67.3	35.4	64.9	70.0	81.3	43.4
Synthetic + Real (100%)	100%	100%	47.6	37.5	<b>69.4</b>	35.9	67.0	70.2	<b>87.2</b>	43.7
	200%	100%	<b>48.9</b>	<b>39.6</b>	69.0	<b>38.2</b>	<b>67.5</b>	<b>70.7</b>	86.1	<b>45.7</b>
	300%	100%	47.9	38.6	68.9	36.2	66.6	70.0	84.9	44.8

### 4.3. Ablation Study

Table 4. Ablation on the latent point cloud space as input to the latent diffusion model (LDM) by removing the VAE component. Comparison of background generation of radar point clouds evaluated on validation set from VoD.

Method	LDM	CD ↓	CD <sub>Doppler</sub> ↓	CD <sub>RCS</sub> ↓
SPVD [37]		3.63	4.80	25.04
<b>Ours</b>	✓	<b>2.26</b>	<b>1.24</b>	<b>6.75</b>

In this ablation study, we verify the effectiveness of departing to the latent space for the diffusion process of radar point clouds. We evaluate the quality of the generated background radar points on the VoD validation set in Tab. 4, comparing diffusion applied on radar point clouds directly with our latent diffusion approach.

We observe that our approach significantly outperforms the vanilla diffusion model across all metrics, showing the benefit of operating the diffusion within the latent space. We also provide a qualitative comparison of both approaches in the supplementary materials. In addition, an ablation on the backbone of our diffusion model can be found in Appendix D.

### 4.4. Limitations

Despite the impressive results in 4D radar point cloud generation, our method still has several limitations. First, our model generates a fixed number of points, which can lead to discrepancies in density between real and generated radar point clouds, as can be seen in the top right of Fig. 3. Second, although separating the generation process for background and foreground points helps maintain high fidelity for each component, this detachment can introduce incon-

sistencies. For example, partial occlusion caused by the environment is not taken into consideration (see Appendix E). Third, our foreground generation does not model the trail of motion produced by dynamic objects when aggregating multiple radar scans. This could be addressed by also compensating the motion of dynamic objects based on Doppler information, as done in [10]. Finally, the background generation is conditioned on LiDAR point cloud data. This imposes various practical constraints, as it requires a high-cost sensor and makes our approach sensor-dependent, limiting generalization across datasets. Leveraging alternative conditioning inputs for the background environment, such as semantic maps or camera images, could be a promising direction.

## 5. Conclusion

In this paper, we have presented a novel latent diffusion framework for generating 4D radar point clouds. The proposed 4D-RaDiff performs diffusion on a latent point cloud representation, conditioned on either 3D bounding boxes or LiDAR point clouds to synthesize corresponding radar points for foreground and background, respectively. Thus, our method can generate radar annotations to support downstream task training. Our experiments demonstrate that synthetic data generated by 4D-RaDiff improves object detection through data augmentation. We also conducted experiments with pre-training strategies on our synthetic data, showing that fine-tuning on minimal real radar data achieves competitive performance. This is particularly valuable given the difficulty and cost of obtaining accurate radar annotations. Overall, 4D-RaDiff provides a scalable solution for acquiring high-quality and diverse training data for radar-based perception, reducing the reliance on extensive manual annotation in autonomous driving.

## References

- [1] Holger Caesar, Varun Bankiti, Alex H Lang, Sourabh Vora, Venice Erin Liong, Qiang Xu, Anush Krishnan, Yu Pan, Giancarlo Baldan, and Oscar Beijbom. nuscenes: A multimodal dataset for autonomous driving. In *Proceedings of the IEEE/CVF conference on computer vision and pattern recognition*, pages 11621–11631, 2020. [1](#), [6](#), [14](#)
- [2] Jooyoung Choi, Sungwon Kim, Yonghyun Jeong, Youngjune Gwon, and Sungroh Yoon. Ilvr: Conditioning method for denoising diffusion probabilistic models. *arXiv preprint arXiv:2108.02938*, 2021. [2](#)
- [3] Prafulla Dhariwal and Alexander Nichol. Diffusion models beat gans on image synthesis. *Advances in neural information processing systems*, 34:8780–8794, 2021. [2](#)
- [4] Jin Fang, Xinxin Zuo, Dingfu Zhou, Shengze Jin, Sen Wang, and Liangjun Zhang. Lidar-aug: A general rendering-based augmentation framework for 3d object detection. In *Proceedings of the IEEE/CVF Conference on Computer Vision and Pattern Recognition*, pages 4710–4720, 2021. [2](#)
- [5] Felix Fent, Philipp Bauerschmidt, and Markus Lienkamp. Radargnn: Transformation invariant graph neural network for radar-based perception. In *Proceedings of the IEEE/CVF Conference on Computer Vision and Pattern Recognition*, pages 182–191, 2023. [1](#)
- [6] Felix Fent, Fabian Kutenreich, Florian Ruch, Farija Rizwin, Stefan Juergens, Lorenz Lechermann, Christian Nissler, Andrea Perl, Ulrich Voll, Min Yan, et al. Man truckscenes: A multimodal dataset for autonomous trucking in diverse conditions. *Advances in Neural Information Processing Systems*, 37:62062–62082, 2024. [2](#), [4](#), [5](#), [14](#), [19](#)
- [7] Golnaz Ghiasi, Yin Cui, Aravind Srinivas, Rui Qian, Tsung-Yi Lin, Ekin D Cubuk, Quoc V Le, and Barret Zoph. Simple copy-paste is a strong data augmentation method for instance segmentation. In *Proceedings of the IEEE/CVF conference on computer vision and pattern recognition*, pages 2918–2928, 2021. [2](#)
- [8] Martin Hahner, Christos Sakaridis, Dengxin Dai, and Luc Van Gool. Fog simulation on real lidar point clouds for 3d object detection in adverse weather. In *Proceedings of the IEEE/CVF international conference on computer vision*, pages 15283–15292, 2021. [2](#)
- [9] Martin Hahner, Christos Sakaridis, Mario Bijelic, Felix Heide, Fisher Yu, Dengxin Dai, and Luc Van Gool. Lidar snowfall simulation for robust 3d object detection. In *Proceedings of the IEEE/CVF conference on computer vision and pattern recognition*, pages 16364–16374, 2022. [2](#)
- [10] Yuval Haitman and Oded Bialer. Doppdrive: Doppler-driven temporal aggregation for improved radar object detection. In *Proceedings of the IEEE/CVF International Conference on Computer Vision*, pages 26085–26094, 2025. [8](#)
- [11] Zeyu Han, Junkai Jiang, Xiaokang Ding, Jiahao Wang, Qingwen Meng, Shaobing Xu, Lei He, and Jianqiang Wang. Denserradar: A 4d millimeter-wave radar point cloud detector based on dense lidar point clouds. In *2024 IEEE 27th International Conference on Intelligent Transportation Systems (ITSC)*, pages 930–936. IEEE, 2024. [1](#)
- [12] Yun He, Xinlin Ren, Danhang Tang, Yinda Zhang, Xiangyang Xue, and Yanwei Fu. Density-preserving deep point cloud compression. In *Proceedings of the IEEE/CVF Conference on Computer Vision and Pattern Recognition*, pages 2333–2342, 2022. [3](#), [12](#), [13](#)
- [13] Sander Elias Magnussen Helgesen, Kazuto Nakashima, Jim Tørresen, and Ryo Kurazume. Fast lidar upsampling using conditional diffusion models. In *2024 33rd IEEE International Conference on Robot and Human Interactive Communication (ROMAN)*, pages 272–277. IEEE, 2024. [3](#)
- [14] Jonathan Ho, Ajay Jain, and Pieter Abbeel. Denoising diffusion probabilistic models. *Advances in neural information processing systems*, 33:6840–6851, 2020. [2](#), [3](#), [12](#)
- [15] Qianjiang Hu, Zhimin Zhang, and Wei Hu. Rangeldm: Fast realistic lidar point cloud generation. In *European Conference on Computer Vision*, pages 115–135. Springer, 2024. [2](#), [3](#)
- [16] Xuzhong Hu, Zaipeng Duan, Xiao Huang, Ziwen Xu, Delie Ming, and Jie Ma. Context-aware data augmentation for lidar 3d object detection. In *2023 IEEE International Conference on Image Processing (ICIP)*, pages 11–15. IEEE, 2023. [2](#)
- [17] Woo-Jin Jung, Dong-Hee Paek, and Seung-Hyun Kong. L2rdas: Synthesizing 4d radar tensors for model generalization via dataset expansion. *arXiv preprint arXiv:2503.03637*, 2025. [6](#)
- [18] Tero Karras, Miika Aittala, Timo Aila, and Samuli Laine. Elucidating the design space of diffusion-based generative models. *Advances in neural information processing systems*, 35:26565–26577, 2022. [2](#)
- [19] Velat Kilic, Deepti Hegde, Vishwanath Sindagi, A Brinton Cooper, Mark A Foster, and Vishal M Patel. Lidar light scattering augmentation (lisa): Physics-based simulation of adverse weather conditions for 3d object detection. *arXiv preprint arXiv:2107.07004*, 2021. [2](#)
- [20] Diederik P Kingma and Max Welling. Auto-encoding variational bayes. In *International Conference on Learning Representations*, 2014. [12](#)
- [21] Ellington Kirby, Mickael Chen, Renaud Marlet, and Nermin Samet. Logen: Toward lidar object generation by point diffusion. *arXiv preprint arXiv:2412.07385*, 2024. [3](#)
- [22] Alex H Lang, Sourabh Vora, Holger Caesar, Lubing Zhou, Jiong Yang, and Oscar Beijbom. Pointpillars: Fast encoders for object detection from point clouds. In *Proceedings of the IEEE/CVF conference on computer vision and pattern recognition*, pages 12697–12705, 2019. [4](#), [5](#), [6](#), [7](#)
- [23] Daeun Lee and Jinkyu Kim. Resolving class imbalance for lidar-based object detector by dynamic weight average and contextual ground truth sampling. In *Proceedings of the IEEE/CVF Winter Conference on Applications of Computer Vision*, pages 682–691, 2023. [2](#)
- [24] Zhijian Liu, Haotian Tang, Yujun Lin, and Song Han. Point-voxel cnn for efficient 3d deep learning. *Advances in neural information processing systems*, 32, 2019. [15](#)
- [25] Kai Luan, Chenghao Shi, Neng Wang, Yuwei Cheng, Huimin Lu, and Xieyuanli Chen. Diffusion-based point cloud super-resolution for mmwave radar data. In *2024 IEEE International Conference on Robotics and Automation (ICRA)*, pages 11171–11177. IEEE, 2024. [1](#), [2](#), [3](#)

- [26] Shentong Mo, Enze Xie, Ruihang Chu, Lanqing Hong, Matthias Niessner, and Zhenguo Li. Dit-3d: Exploring plain diffusion transformers for 3d shape generation. *Advances in neural information processing systems*, 36:67960–67971, 2023. 15
- [27] Kazuto Nakashima and Ryo Kurazume. Lidar data synthesis with denoising diffusion probabilistic models. In *2024 IEEE International Conference on Robotics and Automation (ICRA)*, pages 14724–14731. IEEE, 2024. 2, 3
- [28] Alex Nichol, Prafulla Dhariwal, Aditya Ramesh, Pranav Shyam, Pamela Mishkin, Bob McGrew, Ilya Sutskever, and Mark Chen. Glide: Towards photorealistic image generation and editing with text-guided diffusion models. *arXiv preprint arXiv:2112.10741*, 2021. 2
- [29] Alexander Quinn Nichol and Prafulla Dhariwal. Improved denoising diffusion probabilistic models. In *International conference on machine learning*, pages 8162–8171. PMLR, 2021. 2
- [30] Lucas Nunes, Rodrigo Marcuzzi, Benedikt Mersch, Jens Behley, and Cyrill Stachniss. Scaling diffusion models to real-world 3d lidar scene completion. In *Proceedings of the IEEE/CVF Conference on Computer Vision and Pattern Recognition*, pages 14770–14780, 2024. 2, 3
- [31] Andras Palffy, Jiaao Dong, Julian FP Kooij, and Dariu M Gavrila. Cnn based road user detection using the 3d radar cube. *IEEE Robotics and Automation Letters*, 5(2):1263–1270, 2020. 1
- [32] Andras Palffy, Ewoud Pool, Srimannarayana Baratam, Julian FP Kooij, and Dariu M Gavrila. Multi-class road user detection with 3+ 1d radar in the view-of-delft dataset. *IEEE Robotics and Automation Letters*, 7(2):4961–4968, 2022. 1, 2, 4, 5, 14, 15, 16, 17, 18
- [33] Charles R Qi, Hao Su, Kaichun Mo, and Leonidas J Guibas. Pointnet: Deep learning on point sets for 3d classification and segmentation. In *Proceedings of the IEEE conference on computer vision and pattern recognition*, pages 652–660, 2017. 13
- [34] Aditya Ramesh, Prafulla Dhariwal, Alex Nichol, Casey Chu, and Mark Chen. Hierarchical text-conditional image generation with clip latents. *arXiv preprint arXiv:2204.06125*, 1(2):3, 2022. 2
- [35] Haoxi Ran, Vitor Guizilini, and Yue Wang. Towards realistic scene generation with lidar diffusion models. In *Proceedings of the IEEE/CVF Conference on Computer Vision and Pattern Recognition*, pages 14738–14748, 2024. 2, 3, 15
- [36] Ignacio Roldan, Andras Palffy, Julian FP Kooij, Dariu M Gavrila, Francesco Fioranelli, and Alexander Yarovoy. See further than cfar: a data-driven radar detector trained by lidar. In *2024 IEEE Radar Conference (RadarConf24)*, pages 1–6. IEEE, 2024. 1
- [37] Ioannis Romanelis, Vlassios Fotis, Athanasios Kalogeras, Christos Alexakos, Konstantinos Moustakas, and Adrian Munteanu. Efficient and scalable point cloud generation with sparse point-voxel diffusion models. *arXiv preprint arXiv:2408.06145*, 2024. 3, 8, 15
- [38] Robin Rombach, Andreas Blattmann, Dominik Lorenz, Patrick Esser, and Björn Ommer. High-resolution image synthesis with latent diffusion models. In *Proceedings of the IEEE/CVF conference on computer vision and pattern recognition*, pages 10684–10695, 2022. 2
- [39] Chitwan Saharia, William Chan, Huiwen Chang, Chris Lee, Jonathan Ho, Tim Salimans, David Fleet, and Mohammad Norouzi. Palette: Image-to-image diffusion models. In *ACM SIGGRAPH 2022 conference proceedings*, pages 1–10, 2022. 2
- [40] Chitwan Saharia, William Chan, Saurabh Saxena, Lala Li, Jay Whang, Emily L Denton, Kamyar Ghasemipour, Raphael Gontijo Lopes, Burcu Karagol Ayan, Tim Salimans, et al. Photorealistic text-to-image diffusion models with deep language understanding. *Advances in neural information processing systems*, 35:36479–36494, 2022. 2
- [41] Nicolas Scheiner, Florian Kraus, Nils Appenrodt, Jürgen Dickmann, and Bernhard Sick. Object detection for automotive radar point clouds—a comparison. *AI Perspectives*, 3(1):6, 2021. 1
- [42] Fatih Sezgin, Daniel Vriesman, Dagmar Steinhauser, Robert Lugner, and Thomas Brandmeier. Safe autonomous driving in adverse weather: Sensor evaluation and performance monitoring. In *2023 IEEE Intelligent Vehicles Symposium (IV)*, pages 1–6. IEEE, 2023. 1
- [43] Guangsheng Shi, Ruifeng Li, and Chao Ma. Pillarnet: Real-time and high-performance pillar-based 3d object detection. In *European conference on computer vision*, pages 35–52. Springer, 2022. 5, 6, 7
- [44] Connor Shorten and Taghi M Khoshgoftaar. A survey on image data augmentation for deep learning. *Journal of big data*, 6(1):1–48, 2019. 2
- [45] Jiaming Song, Chenlin Meng, and Stefano Ermon. Denoising diffusion implicit models. In *Proceedings of the 9th International Conference on Learning Representations (ICLR)*, 2021. 2
- [46] Peili Song, Dezhen Song, Yifan Yang, Enfan Lan, and Jingtai Liu. Simulating automotive radar with lidar and camera inputs. *arXiv preprint arXiv:2503.08068*, 2025. 2
- [47] Yang Song, Jascha Sohl-Dickstein, Diederik P Kingma, Abhishek Kumar, Stefano Ermon, and Ben Poole. Score-based generative modeling through stochastic differential equations. In *ICLR*, 2021. 2
- [48] Ashish Vaswani, Noam Shazeer, Niki Parmar, Jakob Uszkoreit, Llion Jones, Aidan N Gomez, Łukasz Kaiser, and Illia Polosukhin. Attention is all you need. *Advances in neural information processing systems*, 30, 2017. 3
- [49] Shengpeng Wang, Xin Luo, Yulong Xie, and Wei Wang. Sd-diff: Boost radar perception via spatial-doppler diffusion. *arXiv preprint arXiv:2506.16936*, 2025. 3
- [50] Jincheng Wu, Ruixu Geng, Yadong Li, Dongheng Zhang, Zhi Lu, Yang Hu, and Yan Chen. Diffiradar: high-quality mmwave radar perception with diffusion probabilistic model. In *ICASSP 2024-2024 IEEE International Conference on Acoustics, Speech and Signal Processing (ICASSP)*, pages 8291–8295. IEEE, 2024. 1, 3
- [51] Ruixin Wu, Zihan Li, Jin Wang, Xiangyu Xu, Zhi Zheng, Kaixiang Huang, and Guodong Lu. Diffusion-based mmwave radar point cloud enhancement driven by range images. *arXiv preprint arXiv:2503.02300*, 2025. 2, 3

- [52] Xiaoyang Wu, Li Jiang, Peng-Shuai Wang, Zhijian Liu, Xihui Liu, Yu Qiao, Wanli Ouyang, Tong He, and Hengshuang Zhao. Point transformer v3: Simpler faster stronger. In *Proceedings of the IEEE/CVF conference on computer vision and pattern recognition*, pages 4840–4851, 2024. 15
- [53] Zhengkang Xiang, Kourosh Khoshelham, and Amir Khodabandeh. L-pcd: Latent-guided point cloud diffusion for lidar object augmentation in driving scenes. *Information Fusion*, page 103886, 2025. 3
- [54] Aoran Xiao, Jiaying Huang, Dayan Guan, Kaiwen Cui, Shijian Lu, and Ling Shao. Polarmix: A general data augmentation technique for lidar point clouds. *Advances in Neural Information Processing Systems*, 35:11035–11048, 2022. 14
- [55] Yan Yan, Yuxing Mao, and Bo Li. Second: Sparsely embedded convolutional detection. *Sensors*, 18(10):3337, 2018. 2, 5, 6, 7
- [56] Yanlong Yang, Jianan Liu, Guanxiong Luo, Hao Li, Eui-joon Ahn, Mostafa Rahimi Azghadi, and Tao Huang. Un-supervised radar point cloud enhancement via arbitrary lidar guided diffusion prior. *arXiv preprint arXiv:2505.09887*, 2025. 3
- [57] Tianwei Yin, Xingyi Zhou, and Philipp Krahenbuhl. Center-based 3d object detection and tracking. In *Proceedings of the IEEE/CVF conference on computer vision and pattern recognition*, pages 11784–11793, 2021. 5, 6, 7, 8, 14
- [58] Keisuke Yoneda, Naoki Suganuma, Ryo Yanase, and Mohammad Aldibaja. Automated driving recognition technologies for adverse weather conditions. *IATSS research*, 43(4): 253–262, 2019. 1
- [59] Sangdoon Yun, Dongyoon Han, Seong Joon Oh, Sanghyuk Chun, Junsuk Choe, and Youngjoon Yoo. Cutmix: Regularization strategy to train strong classifiers with localizable features. In *Proceedings of the IEEE/CVF international conference on computer vision*, pages 6023–6032, 2019. 2
- [60] Hongyi Zhang, Moustapha Cisse, Yann N Dauphin, and David Lopez-Paz. mixup: Beyond empirical risk minimization. In *ICLR*, 2018. 2
- [61] Ruibin Zhang and Fei Gao. Sem-radiff: Diffusion-based 3d radar semantic perception in cluttered agricultural environments. *arXiv preprint arXiv:2509.02283*, 2025. 3
- [62] Ruibin Zhang, Donglai Xue, Yuhan Wang, Ruixu Geng, and Fei Gao. Towards dense and accurate radar perception via efficient cross-modal diffusion model. *IEEE Robotics and Automation Letters*, 2024. 1, 2, 3
- [63] Hengshuang Zhao, Li Jiang, Jiaya Jia, Philip HS Torr, and Vladlen Koltun. Point transformer. In *Proceedings of the IEEE/CVF international conference on computer vision*, pages 16259–16268, 2021. 12, 14, 15
- [64] Boyuan Zheng, Shouyi Lu, Renbo Huang, Mingqing Huang, Fan Lu, Wei Tian, Guirong Zhuo, and Lu Xiong. R2ldm: An efficient 4d radar super-resolution framework leveraging diffusion model. *arXiv preprint arXiv:2503.17097*, 2025. 3
- [65] Guangcong Zheng, Xianpan Zhou, Xuewei Li, Zhongang Qi, Ying Shan, and Xi Li. Layoutdiffusion: Controllable diffusion model for layout-to-image generation. In *Proceedings of the IEEE/CVF Conference on Computer Vision and Pattern Recognition*, pages 22490–22499, 2023. 3, 4
- [66] Yi Zhou, Lulu Liu, Haocheng Zhao, Miguel López-Benítez, Limin Yu, and Yutao Yue. Towards deep radar perception for autonomous driving: Datasets, methods, and challenges. *Sensors*, 22(11):4208, 2022. 1
- [67] Vlas Zyrianov, Henry Che, Zhijian Liu, and Shenlong Wang. Lidardm: Generative lidar simulation in a generated world. *arXiv preprint arXiv:2404.02903*, 2024. 2, 3

# 4D-RaDiff: Latent Diffusion for 4D Radar Point Cloud Generation

## Supplementary Material

This supplementary material is organized as follows:

- In Section A, we provide additional background information on diffusion models.
- In Section B, we describe the architecture and implementation of the variational autoencoder.
- In Section C, we outline further implementation details relevant to our experiments.
- In Section D, we perform an ablation study on the backbone of our latent diffusion model.
- In Section E, we present additional qualitative results.

### A. Diffusion Model Details

Given a sample  $x_0 \sim q(x)$  from a target data distribution, diffusion models [14] apply a fixed forward diffusion process, formulated as a Markov chain:

$$q(x_{1:T}|x_0) = \prod_{t=1}^T q(x_t|x_{t-1}), \quad (2)$$

$$q(x_t|x_{t-1}) = \mathcal{N}(x_t; \sqrt{1 - \beta_t} x_{t-1}, \beta_t I), \quad (3)$$

where noise is gradually added to the input for  $T$  number of steps according to a variance schedule  $\beta_t$ . After  $T$  forward steps, the sample will approximately converge to Gaussian noise:  $q(x_T) \approx \mathcal{N}(0, I)$ . The forward diffusion process can be simplified using the reparameterization trick [20]:

$$q(x_t|x_0) = \mathcal{N}(x_t; \sqrt{\bar{\alpha}_t} x_0, (1 - \bar{\alpha}_t)I), \quad (4)$$

where  $\alpha_t = 1 - \beta_t$  and  $\bar{\alpha}_t = \prod_{s=1}^t \alpha_s$ . This formulation allows sampling  $x_t$  at an arbitrary timestep  $t$  without computing all intermediate steps.

Diffusion models learn to reverse the forward diffusion:

$$p_\theta(x_{0:T}) = p(x_T) \prod_{t=1}^T p_\theta(x_{t-1}|x_t), \quad (5)$$

$$p_\theta(x_{t-1}|x_t) = \mathcal{N}(x_{t-1}; \mu_\theta(x_t, t), \beta_t I), \quad (6)$$

where the mean  $\mu_\theta(x_t, t)$  is defined by the following parameterization:

$$\mu_\theta(x_t, t) = \frac{1}{\sqrt{\alpha_t}} \left( x_t - \frac{\beta_t}{\sqrt{1 - \bar{\alpha}_t}} \epsilon_\theta(x_t, t) \right). \quad (7)$$

In the equation above, the model  $\epsilon_\theta$  is trained for all possible timesteps  $t$  to predict the noise  $\epsilon$  that has been added to a noisy sample  $x_t$ . By doing so, the diffusion model can iteratively denoise a sample after training:

$$x_{t-1} = \frac{1}{\sqrt{\alpha_t}} \left( x_t - \frac{\beta_t}{\sqrt{1 - \bar{\alpha}_t}} \epsilon_\theta(x_t, t) \right) + \sqrt{\beta_t} \mathcal{N}(0, I). \quad (8)$$

Thus, starting the reverse diffusion from a random noise sample  $x_T \sim \mathcal{N}(0, I)$ , the diffusion model iteratively denoises it until a clean generated sample  $x_0$  representative of the target data distribution is obtained.

### B. Variational Autoencoder Implementation

#### B.1. Model Architecture

The implementation of our VAE builds upon the existing work of [12], which implements an autoencoder for LiDAR point cloud compression. Their method encodes point clouds while preserving local geometry and density by using three embeddings: *density embedding*, *local position embedding* and *ancestor embedding*. It also allows for the compression of point-wise features, which is useful in our case for encoding relevant radar features like Doppler and RCS. An overview of our VAE model architecture is shown in Fig. 5.

The encoder consists of several downsampling blocks, where at each stage the radar point cloud gets downsampled by a downsampling factor  $f_s$  using farthest point sampling. At each downsampling stage the collapsed points set  $C(p)$  is computed, which defines the discarded points that have collapsed into its nearest neighbor point  $p$  after downsampling. Each block then computes and aggregates the three separate feature embeddings. The *density embedding* preserves the density of the point cloud by mapping the downsampling factor of each point,  $u = |C(p)|$ , to a  $d$ -dimensional representation using a multi-layer perceptron (MLP). The *local position embedding* captures the distribution of  $C(p)$  by encoding the local offset (direction and distance) of each collapsed point relative to its nearest neighbor. These local features are projected into a  $d$ -dimensional embedding through MLPs and self-attention layers. To pass along information from previous stages, a Point Transformer [63] layer is employed to aggregate features of the collapsed points set  $C(p)$  into the corresponding sampled point  $p$ , producing the  $d$ -dimensional *ancestor embedding*. Finally, an MLP combines all three embeddings into the feature representation for the next stage.

After the final downsampling step, the feature-enriched point cloud is projected into the latent space via an MLP. Sampling from this latent space gives us the latent point cloud representation. Before passing it to the decoder, we compute a more structured point cloud representation by

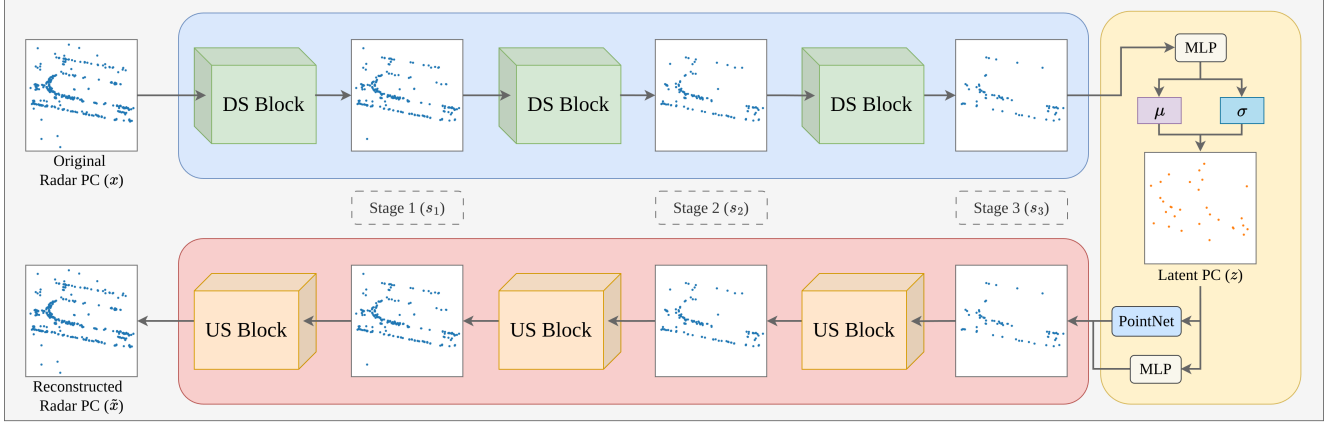


Figure 5. Model architecture of the VAE used in 4D-RaDiff. Downsampling Block (DS) and Upsampling Block (US) are adapted from [12]; please refer to the original paper for details.

obtaining the positional coordinates of each point using a PointNet [33] combined with features from an MLP.

The decoder follows a symmetric design relative to the encoder. At each decoding stage, the decoder block aims to reconstruct the original point cloud corresponding to the input of the matching encoding stage. The decoder block upsamples the downsampled point cloud by predicting an upsampling factor for each point, and then computing local offsets to obtain the upsampled points. After the final upsampling, the reconstructed radar point cloud is obtained, with point-wise features recovered via a segmentation head.

## B.2. Objective Function

To train our VAE, we adopt the distortion loss from [12], and add a Kullback-Leibler (KL) regularization term. The full objective function is thus defined as follows:

$$L_{\text{VAE}} = L_{\text{rec}} + \lambda_{\text{den}} L_{\text{den}} + \lambda_{\text{card}} L_{\text{card}} + \lambda_{\text{reg}} L_{\text{reg}}. \quad (9)$$

Here  $L_{\text{rec}}$  is the reconstruction loss, which encourages the model to accurately reconstruct both the point coordinates  $P \in \mathbb{R}^{N \times 3}$  and their associated point-wise features  $F \in \mathbb{R}^{N \times 2}$  of the original point cloud  $x \in \mathbb{R}^{N \times 5}$ . We define this loss function as:

$$L_{\text{rec}} = L_{\text{CD}}(P, \tilde{P}) + \lambda_c \sum_{s=1}^S L_{\text{CD}}(P_s, \tilde{P}_s) + \lambda_f L_{\text{feat}}(F, \tilde{F}), \quad (10)$$

where we use  $L_{\text{CD}}$ , the Chamfer Distance (CD), to measure the positional difference between the original point cloud 3D coordinates  $P$  and the reconstructed point cloud coordinates  $\tilde{P}$ . Given the symmetric design between our encoder and decoder, we also enforce that the intermediate coordinate reconstructions are similar using a Chamfer Distance

over all  $S$  stages. The CD between two point cloud sets  $A$  and  $B$  is given by:

$$L_{\text{CD}}(A, B) = \frac{1}{|A|} \sum_{a \in A} \min_{b \in B} \|a - b\|_2^2 + \frac{1}{|B|} \sum_{b \in B} \min_{a \in A} \|a - b\|_2^2. \quad (11)$$

Regarding feature reconstruction, we assign each point of the reconstructed point cloud to its nearest ground truth point. Afterwards, we simply compute an L2 loss between the predicted features  $\tilde{F}$  and their assigned ground truth features  $F$ :

$$L_{\text{feat}}(F, \tilde{F}) = \frac{1}{\tilde{N}} \sum_{i=1}^{\tilde{N}} \|f_{\pi(i)} - \tilde{f}_i\|_2^2, \quad (12)$$

where  $\pi(i) = \arg \min_j \|p_j - \tilde{p}_i\|_2$  assigns each reconstructed point  $\tilde{p}_i$  to its nearest ground truth point  $p_j$ .

The density loss  $L_{\text{den}}$  helps to recover the local density when upsampling. At each decoder stage  $s$ , for each point  $\tilde{p}$  we want to predict the correct upsampling factor and the correct local offset to obtain the upsampled points, which is captured by:

$$L_{\text{den}} = \sum_{s=1}^S \sum_{\tilde{p} \in \tilde{P}_s} \frac{|C(p)| - |\tilde{C}(\tilde{p})| + \lambda_d |\overline{C(p)} - \overline{\tilde{C}(\tilde{p})}|}{|\tilde{P}_s|}, \quad (13)$$

where the first term of the numerator measures the difference in the number of points between the downsampled points set  $C(p)$  and the upsampled points set  $\tilde{C}(\tilde{p})$ . The second term computes the difference between the mean distances of all points in each set with respect to their center point  $p$  or  $\tilde{p}$ .

Instead of only computing the density loss between the upsampled and downsampled points sets at each stage  $s$ , we also incorporate a cardinality loss. This loss measures the difference in the number of points between the ground truth point cloud  $P_s$  and the reconstructed point cloud  $\tilde{P}_s$ :

$$L_{card} = \sum_{s=1}^S \left| |P_s| - |\tilde{P}_s| \right|. \quad (14)$$

Lastly, we regularize our latent point cloud space to follow a standard normal distribution using the Kullback-Leibler regularization:

$$L_{reg} = D_{KL}(\mathcal{E}(z|x) \parallel p(z)). \quad (15)$$

## C. Additional Implementation Details

**View-of-Delft (VoD).** For VoD [32], we set our point cloud range to  $[0, 51.2]$ ,  $[-25.6, 25.6]$ ,  $[-3, 2]$  meters for the x, y, and z axes, respectively. Due to the sparsity of radar point clouds, we use five aggregated sweeps of radar point cloud data for all experiments on VoD in the same manner as [32]. This includes training both our generative models and all object detectors. The bounding boxes of VoD do not contain any velocity information, which we require for the foreground generation. Therefore, we adopt a similar approach to nuScenes [1] for obtaining the velocities of the boxes.

**TruckScenes.** For TruckScenes [6], we use a point cloud range of  $[-75, 75]$ ,  $[-75, 75]$  and  $[-2.5, 4.5]$  meters along the x, y, and z axes, respectively. Although the official evaluation includes detection ranges of up to 150 meters for certain classes, we restrict our range to half of this for simplicity and computational efficiency. Nevertheless, this setting still represents a substantially longer range than VoD and contains radar data with 360-degree coverage. In this case, we use six sweeps of radar point clouds following the official implementation of [6]. Since TruckScenes does not provide compensated Doppler features for radar points, we perform ego-motion compensation ourselves to obtain these features.

**Generative Models Training.** We use the following five features for radar point cloud generation: x, y, z, compensated Doppler, and RCS. The compensated Doppler is more intuitive and generally preferred over non-compensated Doppler, as it reflects the true radial velocity of an object by removing the influence of the ego vehicle’s motion. Consequently, it is easier for the LDM to generate accurate compensated Doppler features.

When training our VAE and LDM, we normalize the radar point cloud data globally into  $[-1, 1]$  for all features. To support parallel training with fixed-size batches, we pad or randomly downsample each point cloud sample to match the number of points specified for training. For foreground

generation specifically, the number of points in a scene often falls well below the specified fixed number of points. For example, when a scene only contains one or two bounding boxes with only a few points. In these cases, we augment the scene with additional bounding boxes and points from other samples using a technique similar to PolarMix [54]. The hyperparameters for training our VAE and LDM are listed in Tabs. 5 and 6, respectively.

**Object Detection Training.** We use standard global augmentation techniques for all object detectors during training: random horizontal flip, global rotation within  $[-\pi/4, \pi/4]$ , and global scaling in the range of  $[0.95, 1.05]$ . Most of the annotations of VoD have an unknown difficulty label. Therefore, we do not filter annotations based on difficulty when using GT-Sampling. Moreover, we only insert bounding boxes that contain at least five radar points.

The CenterPoint [57] model is trained on VoD for 80 epochs using a batch size of 32. We use the AdamW optimizer with a weight decay of 0.01 and a one-cycle learning rate policy with a max learning rate of  $1e-3$ .

For TruckScenes dataset, all object detectors are trained for 30 epochs with a batch size of 4. We use the same optimizer and learning rate scheduler as VoD.

**Evaluation Metrics.** We introduce a metric that captures the quality of the generated radar features, i.e., Doppler and RCS. The real radar point cloud is denoted as  $P_{gt} = \{u_1, u_2, \dots, u_n\}$ , and the generated radar point cloud as  $P_{gen} = \{v_1, v_2, \dots, v_m\}$ , where each point  $u_i$  and  $v_j$  consists of a position vector (x, y, z) and feature vector composed of Doppler and RCS values. For each generated point  $v_j \in P_{gen}$ , we find its nearest neighbor in the ground truth point cloud:

$$u_j^* = \arg \min_{u_i \in P_{gt}} \|p(v_j) - p(u_i)\|_2, \quad (16)$$

where  $p(v_j)$  and  $p(u_i)$  denote the 3D positions of  $v_j$  and  $u_i$ , respectively. The generation quality for a single feature  $f$  (Doppler or RCS) is then defined as:

$$CD_f = \frac{1}{m} \sum_{j=1}^m |f(v_j) - f(u_j^*)|. \quad (17)$$

**Training and Sampling Time.** We perform all experiments on a single NVIDIA RTX 4090 GPU. Tab. 7 presents an overview of the average training times and the throughput for each LDM, which is defined as the number of samples generated per second by the model.

## D. Ablation Study on Backbone

We investigate different choices of backbone for our denoising network. Specifically, we consider several architectures used in the point cloud processing or point cloud diffusion literature: PointTransformer (PT) [63], Point Transformer

Table 5. Hyperparameters for VAE training. Batch size differs based on foreground / background generation task.

Hyperparameter	Value
Number of epochs	300
Batch size	128 / 32
Learning rate	1e-3
Optimizer	Adam
Scheduler	StepLR
step size of StepLR	45
$\gamma$ of StepLR	0.5
KL weight ( $\lambda_{reg}$ )	1e-5
Density weight ( $\lambda_{den}$ )	1e-4
Cardinality weight ( $\lambda_{card}$ )	5e-7
Mean distance weight ( $\lambda_d$ )	50.0
Intermediate chamfer weight ( $\lambda_c$ )	0.1
Feature weight ( $\lambda_f$ )	0.05
Latent point dimension ( $d_z$ )	4

Table 6. Hyperparameters for latent diffusion model training. Batch size differs based on foreground / background generation task.

Hyperparameter	Value
Number of epochs	1000
Batch size	128 / 16
Learning rate	1e-4
Optimizer	AdamW
weight decay of AdamW	1e-6
Scheduler	OneCycleLR
Diffusion Parameters	
$\beta_0$	1e-4
$\beta_T$	0.02
$\beta_t$ schedule	Linear
Diffusion Steps $T$	1000

V3 (PTv3) [52], 3D Diffusion Transformers (DiT-3D) [26], Point-Voxel CNN (PVCNN) [24], and Sparse Point-Voxel Diffusion (SPVD) [37]. We evaluate the effectiveness of each backbone based on the generation quality of radar point clouds for the task of unconditional generation. We assess the quality using quantitative metrics such as Jensen-Shannon divergence (JSD) and Minimum Matching Distance (MMD) adapted from LiDAR-based diffusion [35].

From Tab. 8, SPVD achieves slightly better performance than the other methods. However, we note that these quantitative metrics may not be ideal for evaluating unconditional generation of radar point clouds, as they consider only spatial similarity and do not account for radar-specific features. Furthermore, we believe the small differences in the metrics can be attributed to the inherent sparsity of radar point cloud data and the fact that radar points are very noisy. Therefore, we also provide a qualitative comparison of unconditional

Table 7. Training time and throughput ( $T = 1000$  sampling steps) for different models and datasets, FG indicates foreground and BG background.

Model	Dataset	Training Time (h)	Throughput (samples/s)
VAE-FG	VoD	3.75	-
LDM-FG	VoD	13.02	1.07
VAE-BG	VoD	1.67	-
LDM-BG	VoD	29.12	0.25
VAE-FG	TruckScenes	6.83	-
LDM-FG	TruckScenes	18.75	0.85

Table 8. Ablation on backbone of the latent diffusion model. Comparison of unconditional radar point cloud generation on VoD dataset [32]. MMD is multiplied by  $1 \times 10^4$ .

Method	JSD $\downarrow$	MMD $\downarrow$
PT [63]	0.252	6.92
PTv3 [52]	0.243	6.66
DiT-3D [26]	0.245	6.99
PVCNN [24]	0.238	6.41
<b>SPVD [37]</b>	<b>0.233</b>	<b>6.25</b>

radar point cloud generation of the various models in Fig. 7. We observe that SPVD appears to generate more accurate and diverse representations of radar point clouds compared to the other approaches.

## E. Additional Qualitative Results

We present a limitation of our approach in Fig. 6. Since we separate the generation process for background and foreground points, the two components are generated independently. As a result, for bounding boxes that are partially occluded by the environment (background points), our model may still generate foreground points even though the ground truth contains none.

We also provide qualitative results of background generation on the VoD dataset in Fig. 8. In this figure, we compare background points generated by our method against those from the vanilla diffusion model SPVD (DM) used in the ablation study (Sec. 4.3). We can see that the diffusion model captures the overall scene structure, but it produces highly noisy points with unrealistic RCS distributions. In contrast, our method better preserves the fine-grained details of radar point clouds while maintaining realistic RCS values for the radar points.

Moreover, qualitative results of foreground generation on the TruckScenes dataset can be seen in Fig. 9. Our approach generates not only accurate 3D positions for foreground points but also reliable Doppler and RCS values across multiple classes.

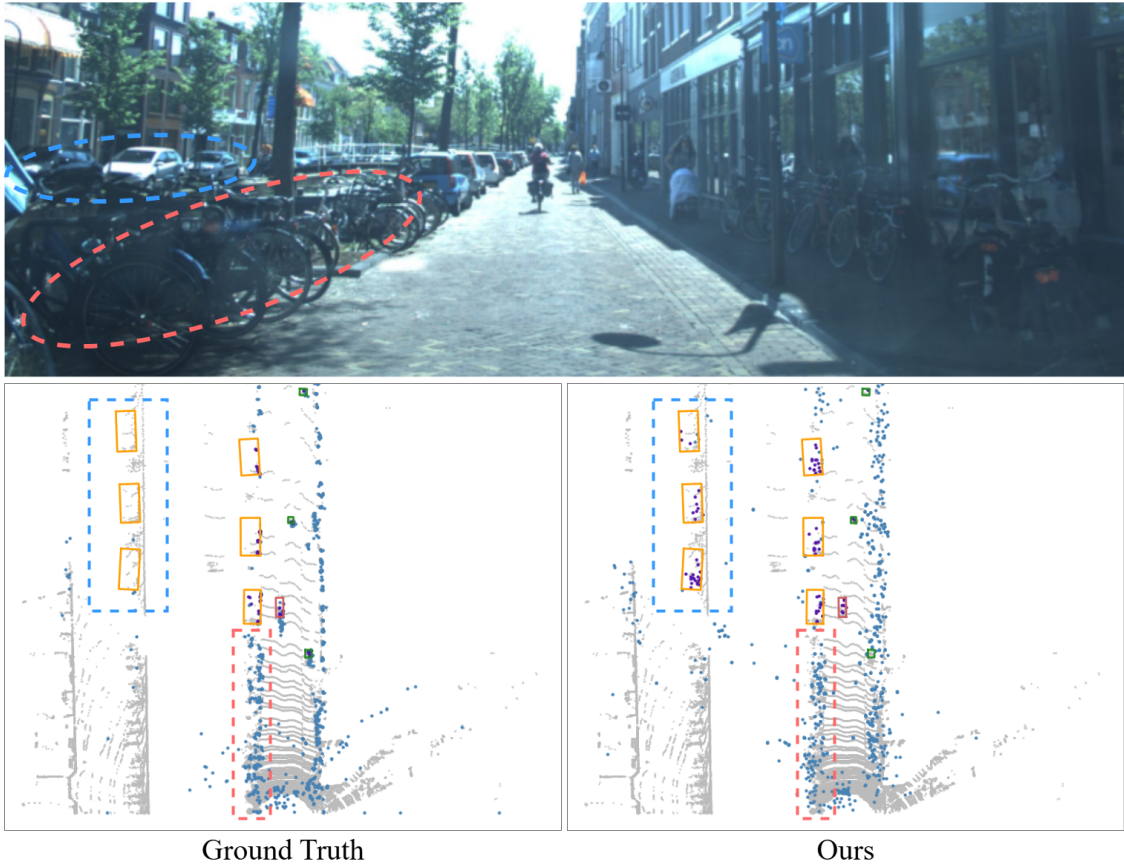


Figure 6. Limitation of our method on VoD [32]. Due to the separation of foreground and background generation, we still generate foreground points for objects (dashed blue) which are partially occluded by the environment (dashed red).

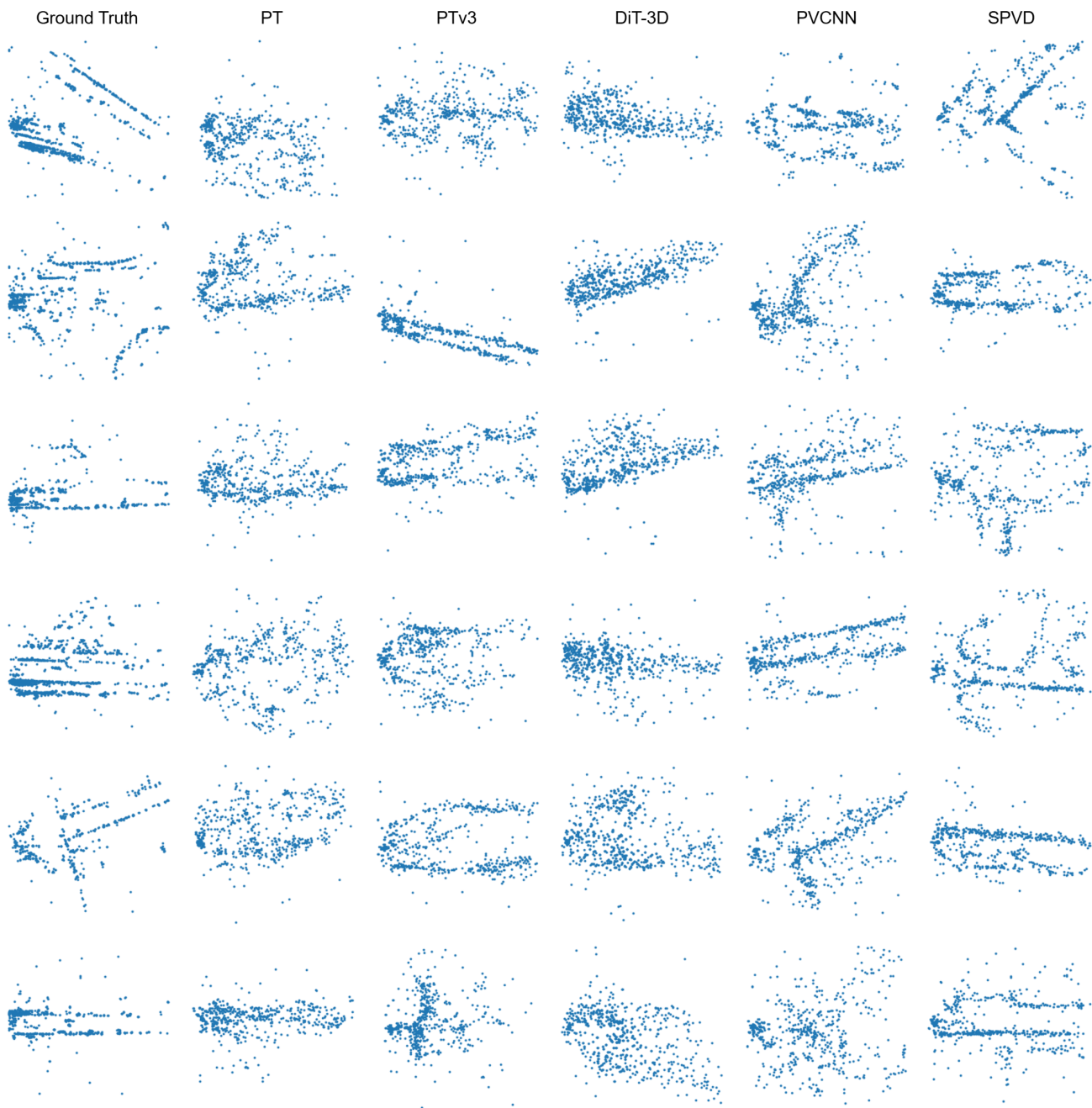


Figure 7. Qualitative results on the VoD dataset [32] of **unconditional** radar point cloud generation using various backbones for the latent diffusion model. All models use the same VAE.

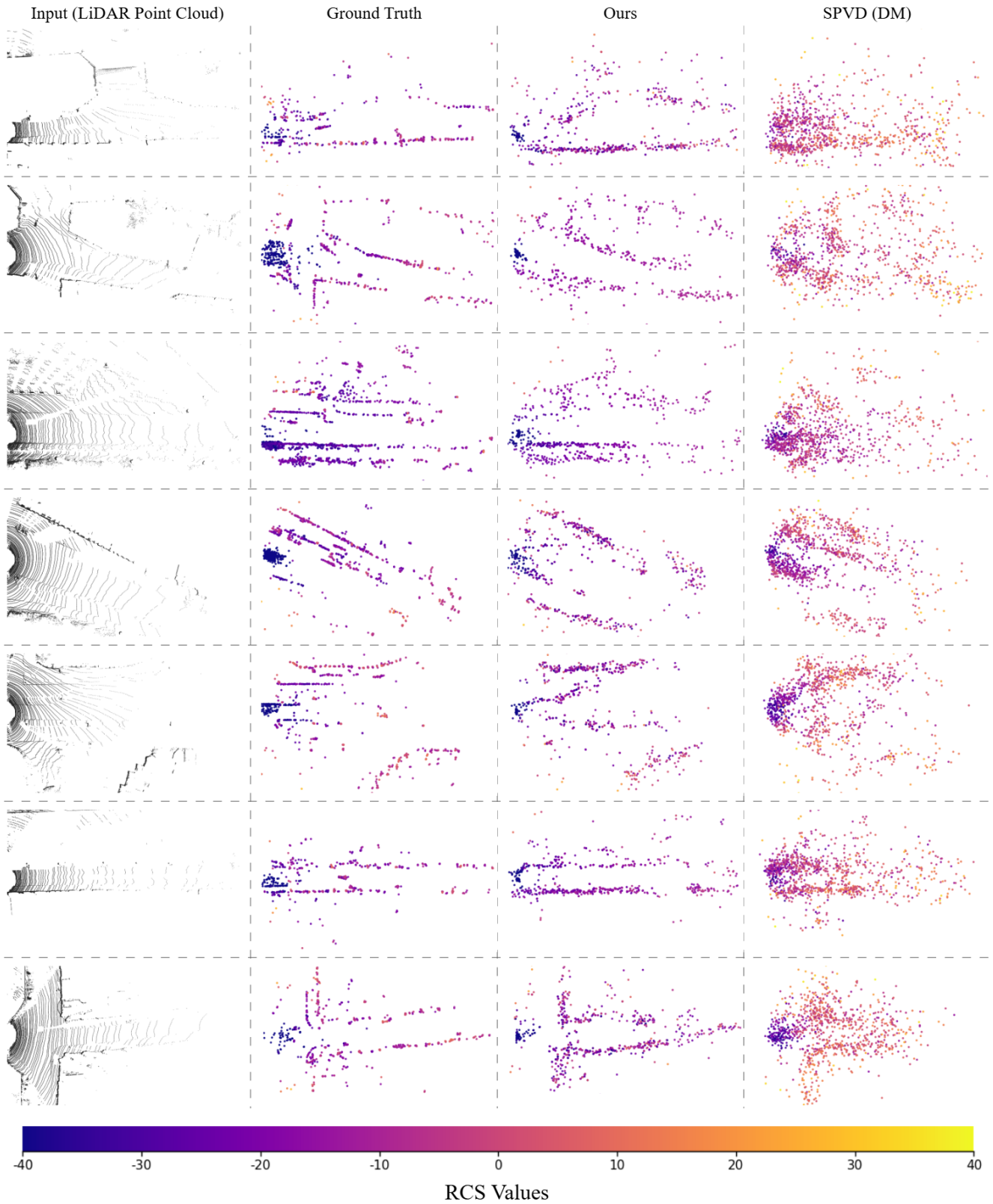


Figure 8. Qualitative results on the VoD dataset [32] of background radar point cloud generation based on LiDAR as conditioning mechanism, radar points are colored by RCS values.

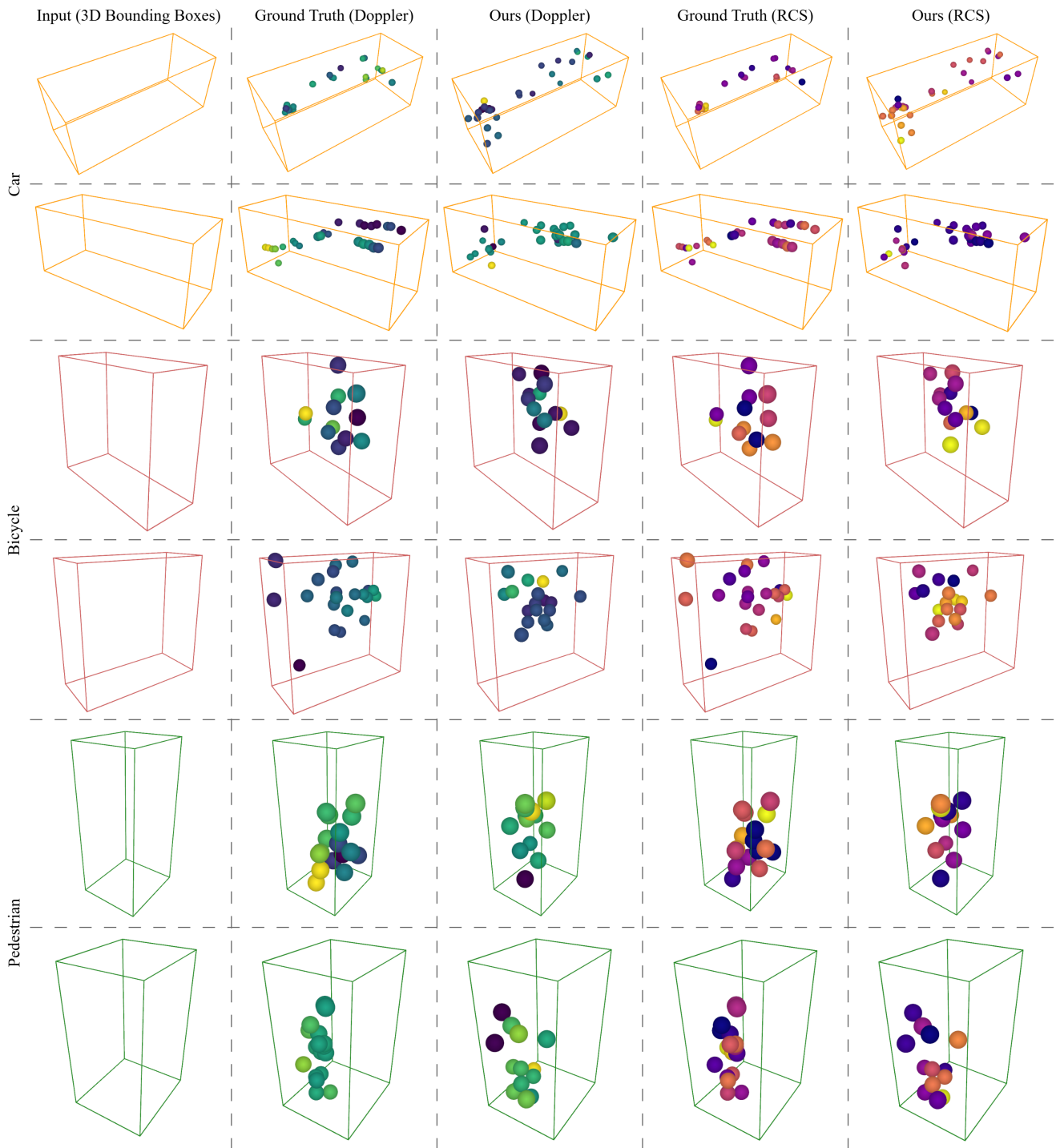


Figure 9. Qualitative results on the TruckScenes dataset [6] of foreground radar point generation based on 3D bounding boxes as conditioning mechanism. Note that for conditioning we actually provide multiple bounding boxes of a scene, but the visualization shows only a single bounding box for clarity. Points are colored by Doppler or RCS (color scale normalized per bounding box).